High-temperature superconductivity in the Ti-H system at high pressures

Jin Zhang, Jeffrey M. McMahon, Artem R. Oganov, Xinfeng Li, Xiao Dong, Huafeng Dong, and Shengnan Wang

Phys. Rev. B **101**, 134108 — Published 17 April 2020

DOI: 10.1103/PhysRevB.101.134108

High-Temperature Superconductivity in the Ti–H System at High Pressures

Jin Zhang and Jeffrey M. McMahon*
Department of Physics and Astronomy, Washington State University, Pullman, WA 99164, USA

Artem R. Oganov†
Skolkovo Institute of Science and Technology, Skolkovo Innovation Center, 3 Nobel St., Moscow, 143026, Russia
Moscow Institute of Physics and Technology, 9 Institutskiy Lane, Dolgoprudny 141700, Russia and
International Center for Materials Discovery, Northwestern Polytechnical University, Xi'an, Shaanxi 710072, PR China

Xinfeng Li
Sino-French Institute of Nuclear Engineering and Technology,
Sun Yat-sen University, Zhuhai, Guangzhou 519082, China

Xiao Dong
Key Laboratory of Weak-Light Nonlinear Photonics and School of Physics, Nankai University, Tianjin 300071, China

Huafeng Dong
School of Physics and Optoelectronic Engineering,
Guangdong University of Technology, Guangzhou 510006, China

Shengnan Wang
Department of Geosciences, Center for Materials by Design,
and Institute for Advanced Computational Science,
State University of New York, Stony Brook, NY 11794-2100, USA

Search for stable high-pressure compounds in the Ti–H system reveals the existence of titanium hydrides with new stoichiometries, including $Ibam$-Ti_2H_5, $I4/m$-Ti_5H_{13}, $I\bar{4}$-Ti_5H_{14}, $Fddd$-TiH_4, $Immm$-Ti_2H_{13}, $P\bar{1}$-TiH_{12}, and $C2/m$-TiH_{22}. Our calculations predict $I4/mmm \rightarrow R\bar{3}m$ and $I4/mmm \rightarrow Cmma$ transitions in TiH and TiH_2, respectively. Phonons and the electron–phonon coupling of all searched titanium hydrides are analyzed at high pressure. It is found that $Immm$-Ti_2H_{13} rather than the highest hydrogen content $C2/m$-TiH_{22}, exhibits the highest superconducting critical temperature T_c. The estimated T_c of $Immm$-Ti_2H_{13} and $C2/m$-TiH_{22} are respectively 127.4–149.4 K (μ^*=0.1-0.15) at 350 GPa and 91.3–110.2 K at 250 GPa by numerically solving the Eliashberg equations.

I. INTRODUCTION

Enthusiasm for discovering high-temperature superconductors never cease[1], since solid mercury was discovered to have zero electrical resistance below 4.2 K in 1911[2]. In recent years, especially at high pressure, the record of the critical temperature (T_c) of superconductivity has been quickly and repeated to be broken in both experimental and theoretical studies, rendering the ultimate goal for synthesizing a room-temperature superconductor (T_c at around 298 K) appears to be within reach. In 2014, first-principles calculation[3] based on density functional theory (DFT) predicted the T_c of $Im\bar{3}m$-H_3S to be around 191 K–204 K at 200 GPa. Subsequently, diamond anvil cell (DAC) experiment in 2015[4] verified this prediction and reported the T_c of sulfur hydride of 203 K by compressing hydrogen sulfide to 150 GPa. In 2017, DFT calculation[5] estimated T_c of $Fm\bar{3}m$-LaH_{10} to be 274–286 K at 210 GPa and of $Fm\bar{3}m$-YH_{10} to be 305–326 K (the highest theoretically-calculated T_c for simple binary systems so far[6]) at 250 GPa. Soon afterwards, the teams of Hemley[7] and Eremets[8] observed lanthanum hydride ($Fm\bar{3}m$-LaH_{10}) superconducting under the pressure (170-200 GPa) at around 250–260 K, which is the highest T_c that has been experimentally confirmed. Although the effect of pressure on superconductivity is not fully understood[9,10], these new record high-T_c superconductors are conventional, phonon-mediated ones. Based on Bardeen–Cooper–Schrieffer (BCS) or Migdal–Eliashberg theories, the pressure affects the T_c of conventional superconductors by making impact on their electronic and phonon parameters, e.g. electronic density of states at the Fermi level, average phonon frequency, and electron-phonon coupling (EPC) constant.

Motivation for investigating superconductivity of hydrides under pressure originally came from both the possibility that metallic hydrogen under high pressure could be a high-temperature superconductor[11] and from the viewpoint that the pressure of metallization of hydrogen-rich solids can be considerably lower than that of pure hydrogen[12,13]. Since carrying out the high-pressure experiments is expensive and technically challenging, many of the investigations on these superconductors are performed using calculations and crystal structure prediction techniques. Besides $Im\bar{3}m$-H_3S, $Fm\bar{3}m$-LaH_{10} and $Fm\bar{3}m$-YH_{10} (mentioned above), the calculated T_c of some predicted structures are as follows: $R\bar{3}m$-LiH_6 is 82 K at 300 GPa[14], $Im\bar{3}m$-MgH_6 is 271 K at 400 GPa[15], $Im\bar{3}m$-CaH_6 is 220–235 K at 150 GPa[16], $I4_1md$-ScH_9 is 233 K at 300 GPa[17], $Cmcm$-ZrH is 11 K at 120 GPa[18], $P2_1/m$-HfH_2 is 11–13 K at 260 GPa[19], $Fdd2$-TaH_6 is 124–136 K at 300 GPa[20], $Pm\bar{3}n$-GeH_3 is 140 K at 180 GPa[21], $P6/mmm$-LaH_{16} is 156 K at 200 GPa[22], $C2/m$-SnH_{14} is 86–97 K at 300 GPa[23], $Im\bar{3}m$-H_3Se is 131 at 200 GPa[24], $P6/mmm$-H_4Te is 95–104 at 170 GPa[25]. Almost all binary hydrides systems have been computationally studied by now, at least crudely, see an overview in Ref. 26.

Transition metal hydrides can form a variety of stable stoichiometries and have lower metallization pressure compared with other hydrides. Especially, those with high hydrogen content often contain unexpected hydrogen groups and exhibit intriguing properties. Titanium is such transition metal that inspires us to study the titanium hydrides under high pressure. At ambient conditions, TiH_2 crystallizes in a tetragonal structure ($I4/mmm$), which transforms into a cubic phase ($Fm\bar{3}m$) at temperature increasing to 310 K[27,28]. DAC experiments[29–31] indicated that $I4/mmm$-TiH_2 remains stable at the pressure up to 90 GPa at ambient temperature. The theoretically estimated T_c is 6.7 K (λ=0.84, μ^*=0.1) for $Fm\bar{3}m$-TiH_2 and 2 mK (λ=0.22, μ^*=0.1) for $I4/mmm$-TiH_2[32] at ambient pressure.

In this paper, the crystal structures and superconductivity of titanium hydrides at pressures up to 350 GPa are systematically studied. In addition to $I4/mmm$-TiH_2, several new stoichiometries and phases are found at high pressure by a first-principles evolutionary algorithm. The predicted TiH_{22} becomes thermodynamically stable at pressure above 235 GPa and contains H_{20} units in its crystal structure. The dynamical stability of all high-pressure phases was verified by calculations of phonons throughout the Brillouin zone. Three different approaches are utilized to determine the superconducting T_c. The predicted T_c (numerical solution from the Eliashberg equations) for $C2/m$-TiH_{22} and $Immm$-Ti_2H_{13} are 91.3–110.2 K (at 250 GPa) and 127.4–149.4 K (at 350 GPa), respectively. Our work provides clear guidance for future experimental investigation of potential high-temperature superconductivity in titanium hydrides under pressure.

II. COMPUTATIONAL METHODOLOGY

Variable-compositional prediction of stable compounds in the Ti–H system was performed at 0, 50, 100, 150, 200, 250, 300, and 350 GPa with 24 atoms in the unit cell through first-principles evolutionary algorithm (EA), as implemented in the USPEX code[33–35]. In addition, fixed-compositional structure searches were performed for TiH_{24}, TiH_{26}, and TiH_{28} at 350 GPa. Structure relaxations were based on DFT within the Perdew–Burke–Ernzerhof (PBE) generalized gradient approximation (GGA) exchange–correlation functional[36], as implemented in the VASP package[37]. For each crystal structure search, the maximum number of generations was all set to 80. The initial generation consisting of 120 structures was created using random symmetric generator. Each subsequent generation contained 100 structures produced from the previous generation using heredity (40%), lattice mutation (20%), random symmetric generator (20%) and transmutation (20%) operators. The composition-distribution searched at different pressures is illustrated in the Fig. S1 in the Supplemental Material[38]. The electron–ion interaction was described by projector-augmented wave (PAW) potentials[39,40], with $3p^64s^23d^4$ and $1s^2$ shells treated as valence for Ti and H, respectively. Structures predicted to be stable or low-enthalpy metastable were then carefully reoptimized (the threshold of energy and ionic-force convergences were set to 10^{-8} eV and 10^{-6} eV/Å, respectively) to construct convex hull and phase diagram at each pressure. Brillouin zone (BZ) was sampled using Γ-centered uniform k-meshes ($2\pi \times 0.05$ Å^{-1}) and the kinetic energy cutoff for the plane-wave basis set was 600 eV.

Phonon calculations were carried out using the finite-displacement method as implemented in the Phonopy[41] codes, using VASP to calculate the force constants matrix, as well as density functional perturbation theory (DFPT)[42] in the QUANTUM ESPRESSO (QE) package[43,44]. Results of these two methods were in perfect agreement. The EPC coefficients were calculated using DFPT in QE, the norm-conserving pseudopotentials (tested by comparing the phonon spectra with the results calculated from Phonopy codes) and the PBE functional were used. Convergence tests show that 120 Ry is a suitable cutoff energy for the plane wave basis set in the QE calculation. A 4×4×4 q-mesh was used in the phonon and electron–phonon calculations.

T_c is estimated using three approaches: by numerically solving Eliashberg equations, and solving modified McMillan and Allen–Dynes formulas. Starting from BCS theory, several first-principles Green's function methods had been proposed to calculate the superconducting properties. Migdal–Eliashberg formalism is one of these, and can accurately describe conventional superconductors[45]. Within the Migdal approximation[46], the adiabatic ratio $\lambda\omega_D/\epsilon_F$ ($\simeq\sqrt{m^*/M}$) is small, since the vertex correction O($\sqrt{m^*/M}$) can compare to the bare vertex and then be neglected. In the adiabatic ratio, m^* is the electron effective mass, M is the ion mass, ω_D is Debye frequency and ϵ_F is Fermi energy. Then, T_c can be calculated by solving two nonlinear Eliashberg equations[47] (or isotropic gap equations) for the Matsubara gap (or superconducting order parameter) $\Delta_n\equiv\Delta(i\omega_n)$ and electron mass renormalization function (or wavefunction renormalization factor) $Z_n\equiv Z(i\omega_n)$ along the imaginary frequency axis (i=$\sqrt{-1}$),

$$\Delta_n Z_n = \frac{\pi}{\beta}\sum_{m=-M}^{M}\frac{\lambda(\omega_n-\omega_m)-\mu^*\theta(\omega_c-|\omega_m|)}{\sqrt{\omega_m^2+\Delta_m^2}}\Delta_m \quad (1)$$

and

$$Z_n = 1 + \frac{\pi}{\beta\omega_n}\sum_{m=-M}^{M}\frac{\lambda(\omega_n-\omega_m)}{\sqrt{\omega_m^2+\Delta_m^2}}\omega_m, \tag{2}$$

where β=$1/k_BT$, k_B is the Boltzmann constant, μ^* denotes the Coulomb pseudopotential, θ is the Heaviside function, ω_c is the phonon cut off frequency: ω_c=$3\omega_{max}$, ω_{max} is the maximum phonon frequency, ω_n=$(\pi/\beta)(2n$-$1)$ is the nth fermion Matsubara frequency with n=0,±1,±2,..., the pairing kernel for electron–phonon interaction (or, the electron–boson attraction between two electrons interacting around the Fermi energy[47]) possesses the form $\lambda(\omega_n-\omega_m) = 2\int_0^{\omega_{max}}\frac{\alpha^2F(\omega)\omega}{\omega^2+(\omega_n-\omega_m)^2}d\omega$ and $\alpha^2F(\omega)$ represents the Eliashberg spectral function. These two equations are derived with the help of thermodynamic Green's functions and the derivation was given in detail by Allen and Mitrović[48].

The important feature of the gap equations is that all the involved quantities only depend on the normal state, and then can be calculated first principles. At each temperature T, the coupled equations need to be solved iteratively until self-consistency. T_c is defined as the temperature at which the Matsubara gap Δ_n becomes zero. The Eliashberg equations have been solved numerically for 2201 Matsubara frequencies (M=1100), in this paper. A detailed discussion of this numerical method was presented in Refs. 49 and 50.

In addition to the above numerical method, T_c can also be obtained by other two analytical-formulas, which are widely used for their attractive simplicity and success in the case of small λ. The first one was developed by McMillan[51] and later refined by Allen and Dynes[52,53]. This formula is named as Allen–Dynes modified McMillan equation (using $\frac{\omega_{log}}{1.2}$ in place of the prefactor $\frac{\Theta_D}{1.45}$ in McMillan equation) and is given as

$$T_c = \frac{\omega_{log}}{1.20}exp\left(-\frac{1.04(1+\lambda))}{\lambda-\mu^*(1+0.62\lambda)}\right). \tag{3}$$

where the logarithmic average frequency is defined as $\omega_{log} = exp\left(\frac{2}{\lambda}\int_0^{\omega_{max}}\frac{\alpha^2F(\omega)}{\omega}ln(\omega)d\omega\right)$, the isotropic EPC constant, which is a dimensionless measure of the average strength of the EPC, can be defined as: $\lambda = 2\int_0^{\omega_{max}}\frac{\alpha^2F(\omega)}{\omega}d\omega$.

The second analytical formula is established on the basis of Allen–Dynes modified McMillan equation [Eq. 3], but with correction factors. These are added to increase the range of validity to higher values λ and to consider the influence of the shape of spectral density. This formula is named as Allen–Dynes equation and is defined as[53]

$$T_c = f_1f_2\frac{\omega_{log}}{1.20}exp\left(-\frac{1.04(1+\lambda))}{\lambda-\mu^*(1+0.62\lambda)}\right), \tag{4}$$

where f_1 and f_2 are strong coupling correction and shape correction, respectively. These two factors are

$$f_1 = \left\{1+\left[\frac{\lambda}{2.46(1+3.8\mu^*))}\right]^{\frac{3}{2}}\right\}^{\frac{1}{3}} \tag{5}$$

and

$$f_2 = 1+\frac{\left(\frac{\bar{\omega}_2}{\omega_{log}}-1\right)\lambda^2}{\lambda^2+3.312(1+6.3\mu^*)^2\left(\frac{\bar{\omega}_2}{\omega_{log}}\right)^2}, \tag{6}$$

here, $\bar{\omega}_2$ is defines as: $\bar{\omega}_2 = \left(\frac{2}{\lambda}\int_0^{\omega_{max}}\alpha^2F(\omega)\omega d\omega\right)^{\frac{1}{2}}$.

Regardless of which of the above three methods is used to calculate T_c, two main input quantities are needed. One is the Coulomb pseudopotential μ^*, which models the depairing interaction between the electrons. However, μ^* is hard to calculate from first principles. Herein, we used standard values μ^*=0.1 and 0.15. Another one is the Eliashberg spectral function $\alpha^2F(\omega)$, which models the coupling of phonons to electrons on the Fermi surface. $\alpha^2F(\omega)$ can be calculated as[54]

$$\alpha^2F(\omega) = \frac{1}{2\pi N(\epsilon_F)}\sum_{\mathbf{q}\nu}\delta(\omega-\omega_{\mathbf{q}\nu})\frac{\gamma_{\mathbf{q}\nu}}{\omega_{\mathbf{q}\nu}}, \tag{7}$$

where $N(\epsilon_F)$ is the density of states at the Fermi level per unit cell per spin, $\mathbf{q}$ is the wavevector, $\omega_{\mathbf{q}}$ is the $\mathbf{q}$-point weight, $\omega_{\mathbf{q}\nu}$ is the screened phonon frequency, and $\gamma_{\mathbf{q}\nu}$ is the phonon linewidth, which is determined exclusively by the electron–phonon matrix elements $g_{mn}^{\nu}(\mathbf{k},\mathbf{q})$ with states on the Fermi surface, is given as:

$$\begin{aligned}\gamma_{\mathbf{q}\nu} =& \pi\omega_{\mathbf{q}\nu}\sum_{mn}\sum_{\mathbf{k}}\omega_{\mathbf{k}}\left|g_{mn}^{\nu}(\mathbf{k},\mathbf{q})\right|^2\delta(\epsilon_{m,\mathbf{k}+\mathbf{q}}-\epsilon_F)\\ &\times\delta(\epsilon_{n,\mathbf{k}}-\epsilon_F),\end{aligned} \tag{8}$$

where $\omega_{\mathbf{k}}$ is the $\mathbf{k}$-point weight normalized to 2 in order to account for the spin degeneracy in spin-unpolarized calculations. $g_{mn}^{\nu}(\mathbf{k},\mathbf{q})$ is described as:

$$g_{mn}^{\nu}(\mathbf{k},\mathbf{q}) = \left(\frac{\hbar}{2M\omega_{\mathbf{q}\nu}}\right)^{1/2}\langle m,\mathbf{k}+\mathbf{q}|\delta_{\mathbf{q}\nu}V_{SCF}|n,\mathbf{k}\rangle, \tag{9}$$

here, $|n,k\rangle$ is the bare electronic Bloch state, M is the ionic mass, and $\delta_{\mathbf{q}\nu}V_{SCF}$ is the derivative of the self-consistent potential with respect to the collective ionic displacement corresponding to the phonon wavevector $\mathbf{q}$ and mode ν. In this work, $g_{mn}^{\nu}(\mathbf{k},\mathbf{q})$ is calculated within the harmonic approximation, using QE package.

III. RESULTS AND DISCUSSIONS

Thermodynamic convex hulls for the Ti–H system at several pressures are shown in Fig. 1. In our structure searching, experimentally reported $I4/mmm$-TiH_2

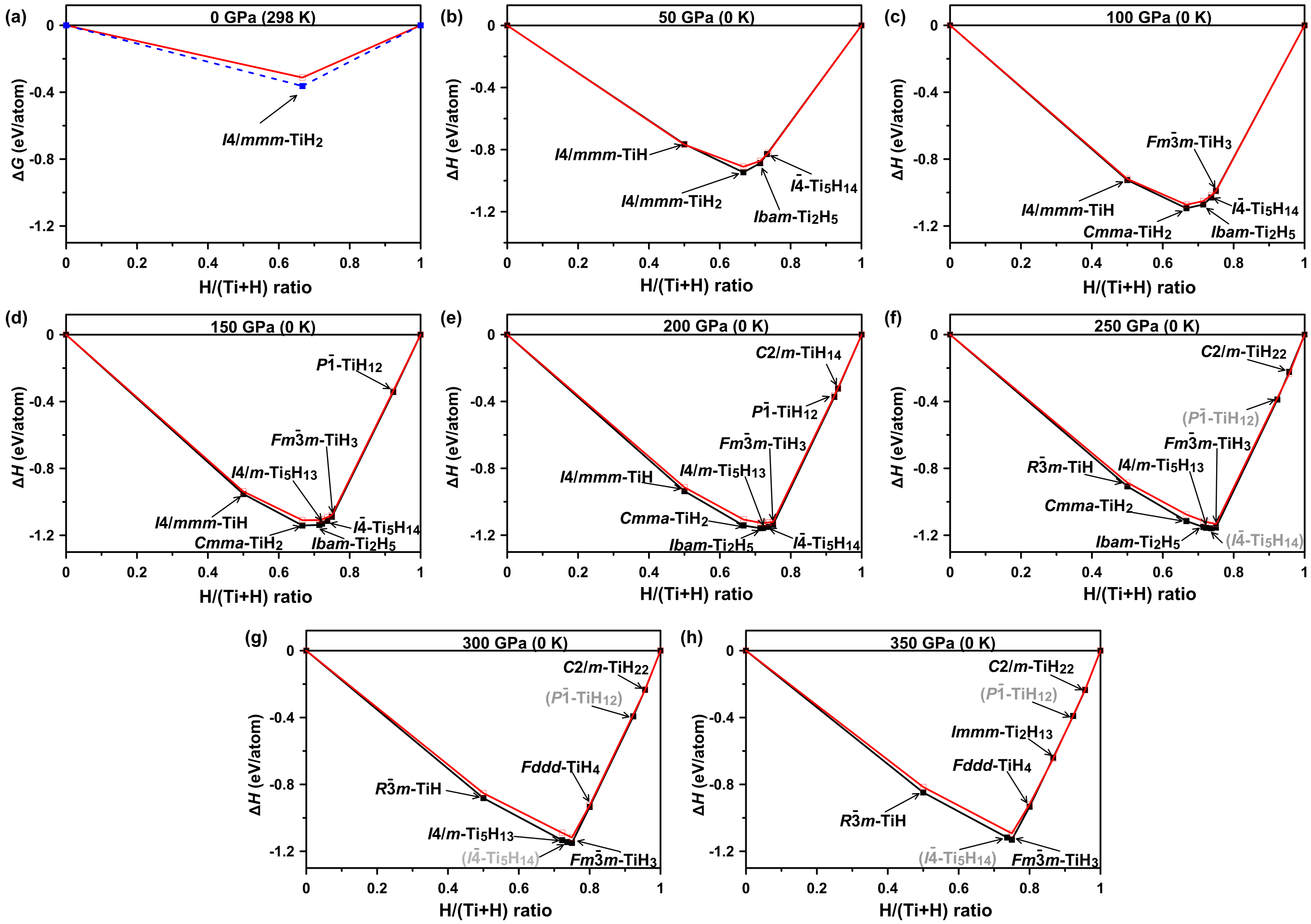

FIG. 1: (Color online) Convex-hull diagrams for the Ti–H system at (a) 0, (b) 50, (c) 100, (d) 150, (e) 200, (f) 250, (g) 300, and (h) 350 GPa. The blue dashed convex hull at 0 GPa shows the experimental result[55]. Black lines with solid squares and red lines with open squares, respectively, represent the calculated results without and with ZPE. The structures indicted in grey are those that lose stability after considering ZPE.

is found to be the only stable phase at zero pressure. Lattice parameters were optimized to be a=3.208 Å and c=4.203 Å at 0 GPa, which is in good accordance with the experimental data (a=3.163 Å and c=4.391 Å)[29]. The calculated Gibbs free energy of formation of $I4/mmm$-TiH_2 is -0.3123 eV/atom at zero pressure and 298 K [red convex hull in Fig. 1(a)], which is in good agreement with the experimental value of -0.363 eV/atom[55] [blue dashed convex hull in Fig. 1(a)]. Besides $I4/mmm$-TiH and $Fm\bar{3}m$-TiH_3, which were already predicted by Zhuang[56] under high pressure, several other phases and stoichiometries, including $R\bar{3}m$-TiH, $Cmma$-TiH_2, $Ibam$-Ti_2H_5, $I4/m$-Ti_5H_{13}, $I\bar{4}$-Ti_5H_{14}, $Fddd$-TiH_4, $Immm$-Ti_2H_{13}, $P\bar{1}$-TiH_{12}, $C2/m$-TiH_{14} and $C2/m$-TiH_{22}, are predicated at pressures up to 350 GPa. No subhydrides (Ti_xH_y, $x > y$) show up in the Ti–H system at any pressure. The enthalpies of formation with and without including zero-point energy (ZPE) are depicted by red lines with open squares and black lines with solid squares in Fig. 1(b)–(h), respectively. Taking ZPE into account did not significantly change the basic shape of convex hulls, but did introduce some changes of the data at pressures above 250 GPa: considering ZPE made $I\bar{4}$-Ti_5H_{14} and $P\bar{1}$-TiH_{12} metastable [indicated in grey in Fig. 1(f)–(h)] instead of stable structures above 250 GPa.

The pressure–composition phase diagram of Ti–H system is depicted in Fig. 2. Based on our calculations, the phase transition sequence of Ti under high pressure is $P6/mmm(\omega) \xrightarrow{104\text{ GPa}} Cmcm(\gamma) \xrightarrow{109\text{ GPa}} Cmcm(\delta) \xrightarrow{127\text{ GPa}} Im\bar{3}m(\beta)$. Although both γ-Ti and δ-Ti have the same space group and contain 4 titanium atoms in their unit cell, the structure of γ-Ti is a distortion of ω-Ti (hcp), while δ-Ti, which is a body-centered one, is more similar to β-Ti (bcc). Under high pressure, $P6_3/m$-H transforms into $C2/c$-H at 110 GPa and further into $Cmca$-H at 280 GPa. The crystal structures of these high-pressure structures are shown in Fig. 4, and

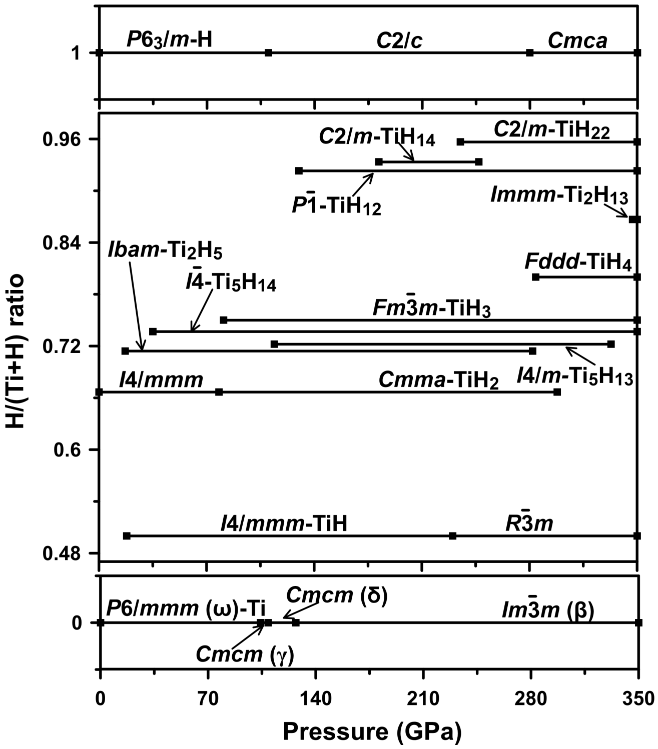

FIG. 2: (Color online) Pressure–composition phase diagram of the Ti–H system at pressure up to 350 GPa.

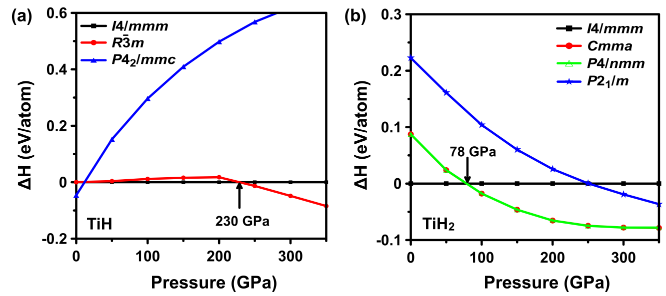

FIG. 3: (Color online) Enthalpy as a function of pressure (without ZPE) for phases of (a) TiH, referenced to the $I4/mmm$-TiH phase, and (b) TiH_2, referenced to the $I4/mmm$-TiH_2 one.

their structural parameters are listed in the Table S1 in Supplemental Material[38].

For TiH, it should be noted that the enthalpy of $P4_2/mmc$-TiH is lower than that of $I4/mmm$-TiH between 0-8 GPa [see also Fig. 3] which is consistent with the aforementioned calculation[56]. However, $P4_2/mmc$-TiH is not thermodynamically stable from 0 to 8 GPa. With pressure increasing to 18 GPa, TiH ($I4/mmm$) begins to become stable and transforms into $R\bar{3}m$-TiH at 230 GPa. In addition, the calculations reveal a tetragonal ($I4/mmm$) to orthorhombic ($Cmma$) phase transition in TiH_2 at 78 GPa. The high-pressure $Cmma$-TiH_2 persists up to 298 GPa, above which TiH_2 is unstable. Note that enthalpy difference of $Cmma$-TiH_2 and $P4/nmm$-TiH_2 is very small, due to the similarity of these two structures.

The structure of $Fm\bar{3}m$-TiH_3 has an fcc-sublattice of Ti atoms, all octahedral and tetrahedral voids of which are occupied by H atoms. It appears at 81 GPa, and continues to be stable up to at least 350 GPa. $Immm$-TiH_6, which is reported to be stabilized above 175 GPa[56], is actually a metastable phase and decomposes into $Fm\bar{3}m$-TiH_3 and $P\bar{1}$-TiH_{12} at high pressure according to our results. Ti_2H_{13}, a stoichiometry close to TiH_6, emerges on the phase diagram at 347 GPa and adopts a $Immm$ structure. TiH_{14} is stable from 182 to 247 GPa. Although both TiH_{14} and SnH_{14}[23] crystallize in $C2/m$ space group, their structures and their hydrogen sublattices are different.

The structure of $Fddd$-TiH_4 consists of titanium atoms which are sandwiched between two slightly distorted H-graphene layers [Fig. 5(b)] in different orientations, forming a $AA_1A_2A_3AA_1A_2A_3A$... stacking sequence [Fig. 5(a)]. The distorted H-graphene layer is drawn in Fig. 5(c); the distance between two layers is 1.373 Å at 350 GPa, as seen in Fig. 5(b). Another interesting part is that besides hydrogen-rich TiH_{14} stoichiometry mentioned above, an *extremely* H-rich structure TiH_{22} is identified to be thermodynamically stable in a monoclinic structure at pressures above 235 GPa. To the best of our knowledge, $C2/m$-TiH_{22} presently is the second hydrogen-richest hydrides known or predicted to date, after metal hydride $C2/c$-YH_{24}[57]. The polyhedral crystal structure representation of $C2/m$-TiH_{22} [depicted in Fig. 6(a)] exhibits alternations of H_2 molecules and TiH_{20} polyhedra. Titanium is encapsulated in H_{20} cages with Ti-H distances are 1.62–1.66 Å at 350 GPa, as shown in Fig. 6(b). The band structure and density of states (DOS) of $C2/m$-TiH_{22} at 350 GPa [Fig. 6(d)] indicate metallicity of TiH_{22}. The total DOS of $C2/m$-TiH_{22} near the Fermi level $N(\varepsilon_F)$ mostly comes from H atoms, which is opposite to $Fddd$-TiH_4 [Fig. 5(d)]. The coexistence of molecular hydrogen with an H–H distance of 0.819 Å and armchair-like hydrogen chain is clearly revealed by the electron localization function (ELF). As shown in ELF Fig. 6(c), the regions with ELF values of 0.7 include H_2 molecules and armchair-like hydrogen chain, which indicates strong covalent bonding between hydrogen atoms.

Based on the calculated phonon dispersion spectrum at high pressure [displayed in Fig. 7 and Fig. S1],

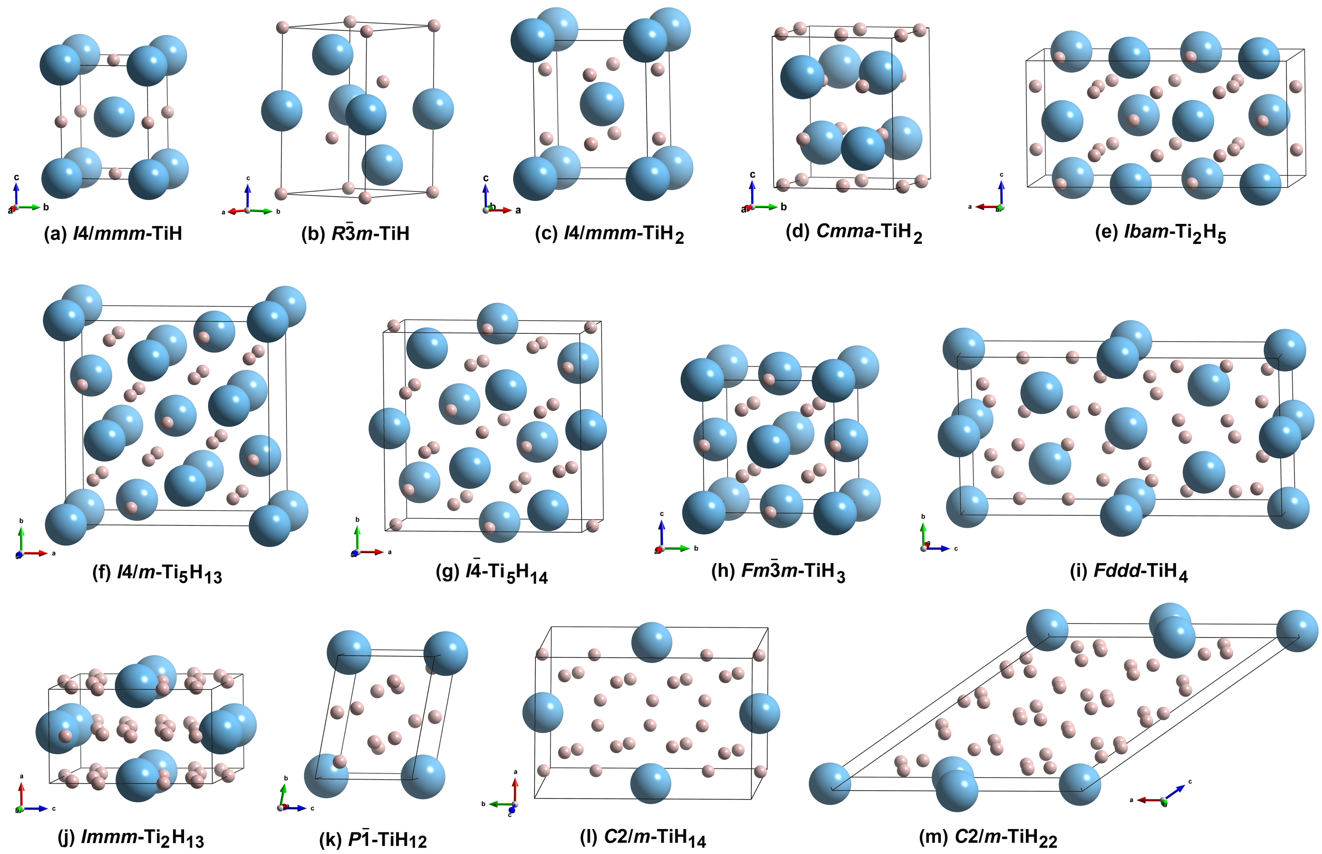

FIG. 4: (Color online) Crystal structures of titanium hydrides. Large spheres represent titanium atoms and small ones represent hydrogen atoms.

no imaginary vibrational frequencies are found in the whole Brillouin zone, indicating the dynamical stability of all the predicted structures. Phonon dispersion curves, phonon density of states, phonon linewidths $\gamma_{\mathbf{q}\nu}$, Eliashberg phonon spectral function $\alpha^2F(\omega)$, and the electron-phonon coupling parameter λ of $Immm$-Ti_2H_{13} , $C2/m$-TiH_{22} , $I\bar{4}$-Ti_5H_{14}, $P\bar{1}$-TiH_{12}, $R\bar{3}m$-TiH and $Fddd$-TiH_4, at selected pressures are depicted in Fig. 7. As expected (due to atomic masses), low-frequency modes are mostly related to Ti atoms whereas high-frequency modes are dominated by vibrations of H ones. Moreover, in all of these six structures, the $\gamma_{\mathbf{q}\nu}$ of branches near the Γ point are much greater than those elsewhere in the Brillouin zone. The total λ of $R\bar{3}m$-TiH is mainly contributed by the acoustic modes, whereas those of the other five structures are dominated by optical branches.

We further probe superconductivity of these hydrides, using BCS theory. The calculated superconducting properties are summarized in Table I. All of the predicted titanium hydrides exhibit superconductivity at high pressures. The highest T_c of titanium hydrides are possessed by $Immm$-Ti_2H_{13}, $C2/m$-TiH_{22}, $I\bar{4}$-Ti_5H_{14}, $P\bar{1}$-TiH_{12}, $R\bar{3}m$-TiH and $Fddd$-TiH_4. $I4/mmm$-TiH_2 exhibits low T_c values (3 mK, μ^*=0.1) at 50 GPa. On the other hand, superconductivity of titanium monohydride (TiH) comes largely from strong coupling of the electrons with Ti vibrations, and coupling with H vibrations becomes more important as H content increases. Intriguingly, it is $Immm$-Ti_2H_{13} instead of $C2/m$-TiH_{22} that possesses the highest T_c among searched titanium hydrides. The results from the previous studies[5,25] suggest higher hydrogen content in the binary hydrides is one of the necessary prerequisites to obtain higher T_c value. This is not necessarily always the case; the hydrogen content in $C2/m$-TiH_{22} is much higher than in $Immm$-Ti_2H_{13}. Indeed, ω_{log} of $C2/m$-TiH_{22} is larger than that of $Immm$-Ti_2H_{13}. However, this is offset by the lower λ of $C2/m$-TiH_{22} (λ=0.861) compared with that of $Immm$-Ti_2H_{13} (λ=1.423). The $\alpha^2F(\omega)$ was used for numerically solving the Eliashberg equations and the obtained T_c of $Immm$-Ti_2H_{13} is in the range 110.4–131.2 K (λ=1.423, μ^*=0.1–0.15) at 350 GPa.

For $Immm$-Ti_2H_{13} at 350 GPa and $C2/m$-TiH_{22} at 250 GPa, the dependence of the maximum value of the order parameter on temperature for selected μ^* is presented in Fig. 8(c) and (f). The maximum value of order parameter

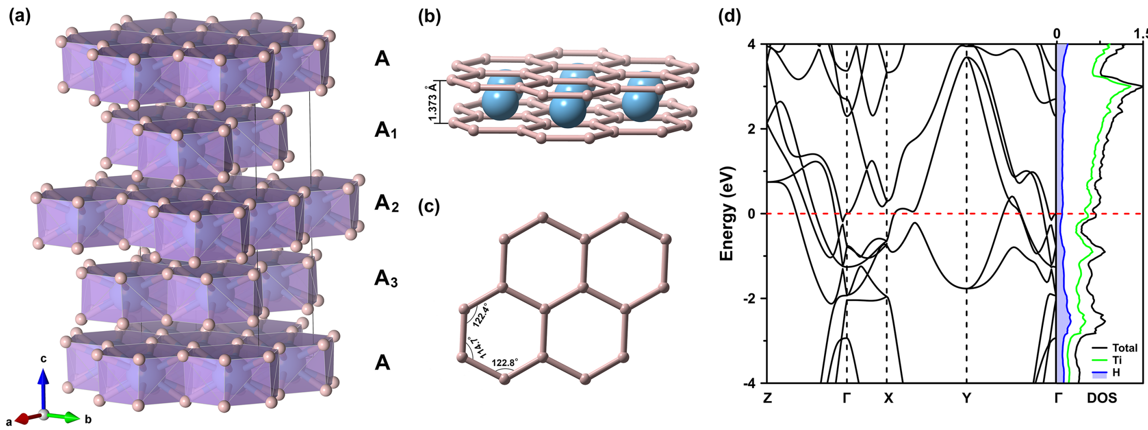

FIG. 5: (Color online) (a) Polyhedral representation of the $Fddd$-TiH_4 structure. Ti-centered hexagonal prisms are shown in purple. (b) The fundamental "sandwich" of TiH_4. (c) Distorted H-graphene layer in $Fddd$-TiH_4, and (d) electronic band structure and density of states (DOS) of $Fddd$-TiH_4 at 300 GPa; DOS is in the unit of states/formula/eV and Fermi energy (red dashed line) is set to zero.

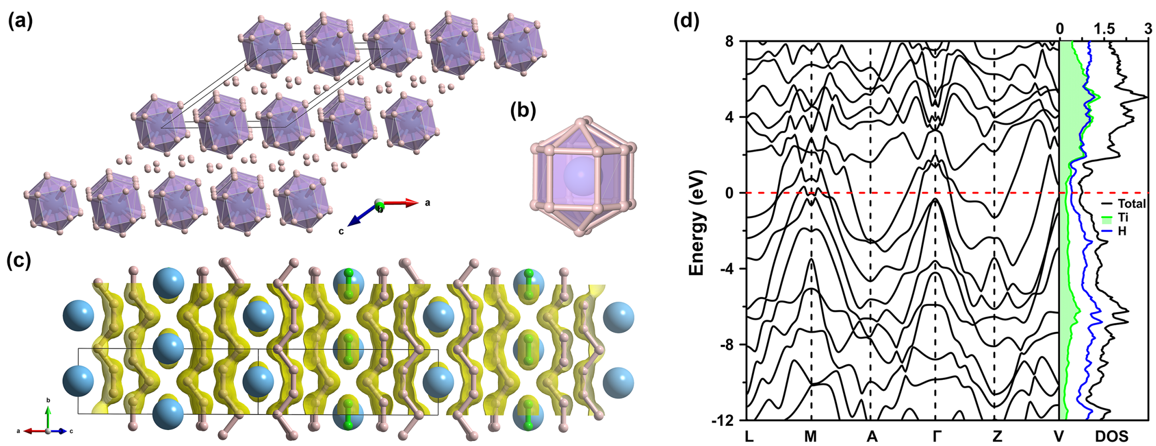

FIG. 6: (Color online) (a) Polyhedral representation of the $C2/m$-TiH_{22} structure. (b) Expanded view of a H_{20} cage encapsulating a Ti atom. (c) ELF isosurface (ELF=0.7) for $C2/m$-TiH_{22} at 350 GPa. Green and pink atoms represent molecular hydrogen and armchair-like hydrogen chains, respectively. (d) Electronic band structure and DOS for $C2/m$-TiH_{22} at 350 GPa.

$\Delta_{m=1}$ decreases with the growth of T and μ^*. On the basis of these results, $\Delta_{m=1}$ value can be characterized analytically by means of the phenomenological formula

$$\Delta_{m=1}(T,\mu^*) = \Delta_{m=1}(T_0,\mu^*)\sqrt{1-\left(\frac{T}{T_c}\right)^{\Gamma}}. \qquad (10)$$

For the maximum value of order parameter $\Delta_{m=1}$, we obtained the estimation of temperature exponent for $Immm$-Ti_2H_{13} (Γ=3.25 for μ^*=0.1; Γ=3.31 for μ^*=0.15) at 250 GPa and $C2/m$-TiH_{22} (Γ=3.21 for μ^*=0.1; Γ=3.16 for μ^*=0.15) at 250 GPa. It is clear that the temperature dependence of maximum order parameter obtained in Eliashberg equations only differs a little bit from the results estimated by the BCS theory, where Γ=3 (Ref. 58). The increase of the Coulomb pseudopotential μ^* leads to a strong decrease of the order parameter [Fig. 8(a) and (d)], with only small perturbations to the wavefunction renormalization factor [Fig. 8(b) and (e)]. This indicates that the influence of the depairing interaction between the electrons is more significant on the energy required to break a Cooper pair (Cooper pairs need to be "broken apart", by giving to the system an energy equal to 2Δ where Δ is the energy gap[59]) than on the enhancement of the electron mass arising from the electron–phonon interaction.

Through comparison among above three approaches of calculating T_c, it can be seen that Allen–Dynes formula much better reproduces the numerical results than the modified McMillan one. Specifically, two analytical equa-

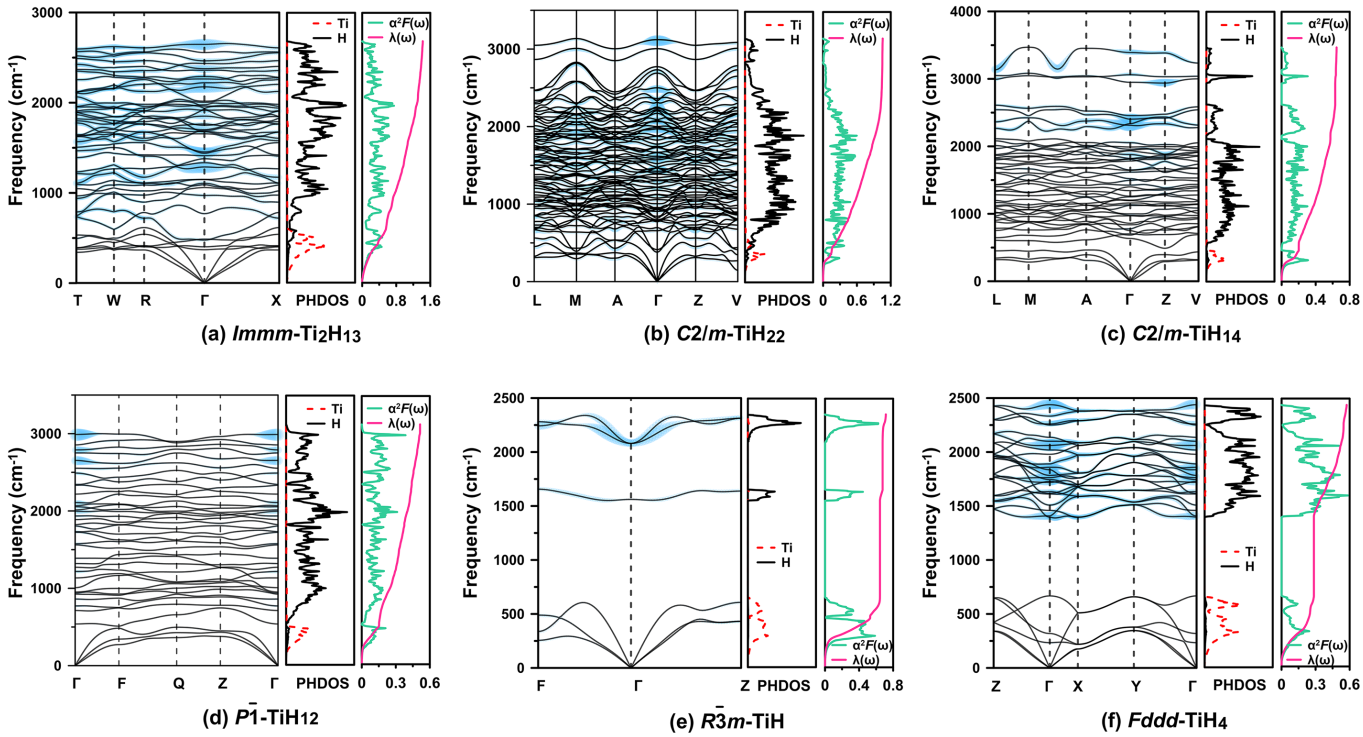

FIG. 7: (Color online) Phonon dispersion curves, phonon density of states projected onto selected atoms, Eliashberg spectral function $\alpha^2F(\omega)$, and the electron–phonon coupling (EPC) parameter λ for (a) $Immm$-Ti_2H_{13} at 350 GPa, (b) $C2/m$-TiH_{22} at 250 GPa, (c) $C2/m$-TiH_{14} at 200 GPa, (d) $P\bar{1}$-TiH_{12} at 350 GPa, (e) $R\bar{3}m$-TiH at 200 GPa and (f) $Fddd$-TiH_4 at 350 GPa. The magnitude of the phonon linewidths is indicated by the size of the blue open circles with the radius proportional to the respective coupling strength.

TABLE I: The EPC parameter λ, electronic density of states at Fermi level $N(\varepsilon_F)$ (states/Ry/cell), the logarithmic average phonon frequency ω_{log} (K) and superconducting critical temperatures T_c (K) for titanium hydrides at different pressure P (GPa). T_c values are given for μ^*=0.1 and T_c in brackets are for μ=0.15; T_c (McM) is the numerical solution of solving the imaginary axis Eliashberg equation, T_c (A–D) is calculated from the Allen–Dynes equation and T_c (E) is obtained by Allen–Dynes modified McMillan equation.

Compound	P	λ	$N(\varepsilon_F)$	ω_{log}	T_c (E)	T_c (A–D)	T_c (McM)
$C2/m$-TiH_{22}	350	0.861	4.765	1677.4	90.7 (65.0)	93.6 (67.3)	100.0 (78.4)
	250	1.057	4.867	1296.2	98.1 (76.7)	103.1 (80.7)	110.2 (91.3)
$C2/m$-TiH_{14}	200	0.645	5.243	1201.7	33.9 (19.7)	35.0 (20.3)	35.9 (25.0)
$P\bar{1}$-TiH_{12}	350	0.514	3.213	1357.6	18.4 (7.8)	18.8 (8.0)	19.5 (11.5)
	150	0.403	3.748	1074.8	4.7 (1.0)	4.8 (1.0)	5.4 (2.4)
$Immm$-Ti_2H_{13}	350	1.423	10.028	1101.3	119.3 (100.8)	131.2 (110.4)	149.4 (127.4)
$Fddd$-TiH_4	350	0.574	3.803	1034.4	20.6 (10.4)	21.2 (10.7)	20.1 (6.2)
$Fm\bar{3}m$-TiH_3	100	0.528	6.798	459.4	6.9 (3.1)	7.1 (3.1)	7.5 (4.7)
$I\bar{4}$-Ti_5H_{14}	350	0.411	20.738	479.9	2.4 (0.6)	2.4 (0.6)	2.8 (1.4)
	50	0.477	35.785	525.6	5.3 (1.9)	5.4 (2.0)	5.8 (3.3)
$I4/m$-Ti_5H_{13}	300	0.470	22.211	412.6	3.9 (1.4)	4.0 (1.4)	4.4 (2.7)
	150	0.406	27.253	450.8	2.1 (0.5)	2.1 (0.5)	2.5 (1.1)
$Ibam$-Ti_2H_5	250	0.504	9.910	363.3	4.6 (1.9)	4.7 (1.9)	5.1 (3.2)
	50	0.564	12.852	365.0	6.9 (3.4)	7.1 (3.5)	6.9 (4.6)
$Cmma$-TiH_2	250	0.509	3.604	434.3	5.7 (2.4)	5.8 (2.4)	6.0 (3.7)
$I4/mmm$-TiH_2	50	0.227	3.687	349.4	0.0 (0.0)	0.0 (0.0)	0.0 (0.0)
$R\bar{3}m$-TiH	350	0.714	4.328	597.3	21.8 (13.9)	22.7 (14.4)	23.9 (18.2)
$I4/mmm$-TiH	200	0.991	6.303	264.3	18.1 (13.8)	19.5 (14.8)	22.5 (18.9)
	50	1.013	8.716	71.0	5.0 (3.9)	5.4 (4.1)	12.6 (10.0)

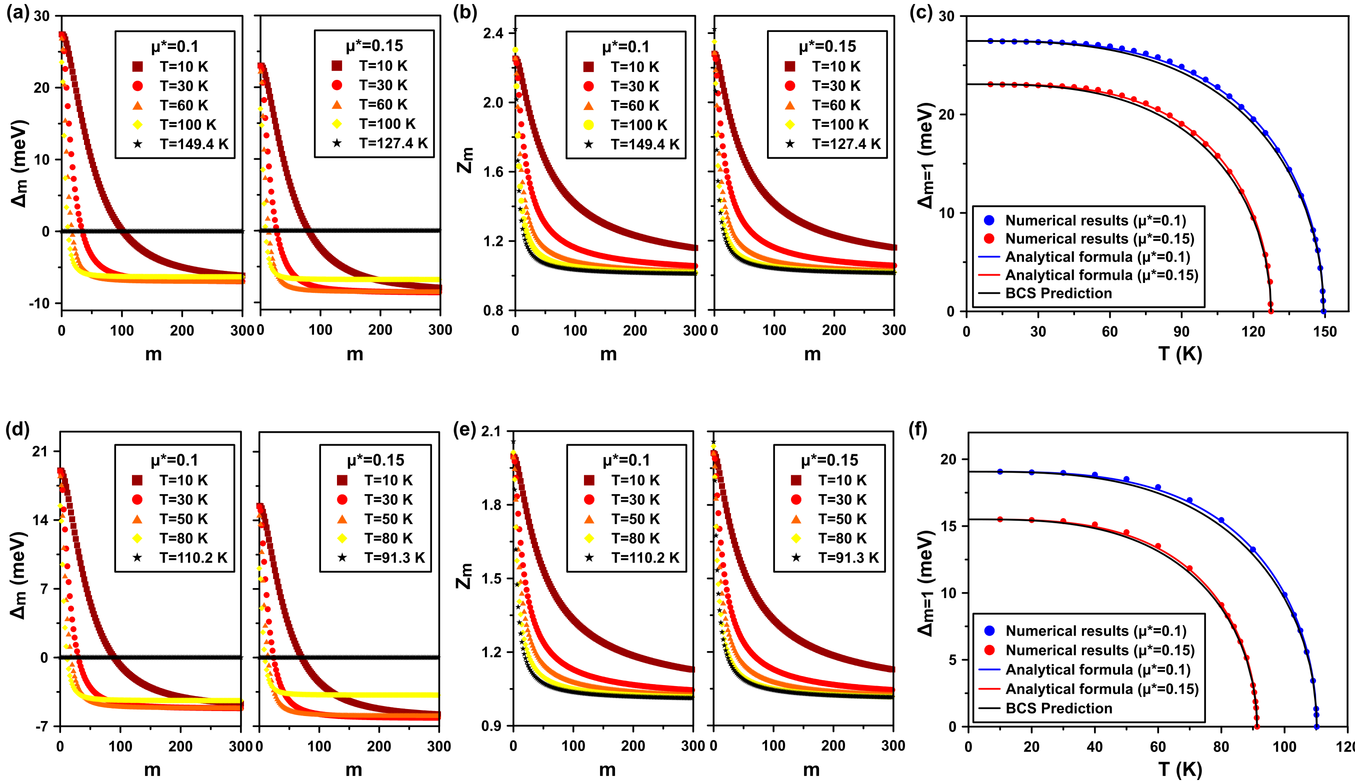

FIG. 8: (Color online) Dependence of the superconducting order parameter on the number m for select values of temperature and Coulomb pseudopotential for (a) *Immm*-Ti_2H_{13} at 350 GPa and (d) $C2/m$-TiH_{22} at 250 GPa. The wave function renormalization factor Z_m on the imaginary axis for select values of temperature and Coulomb pseudopotential for (b) *Immm*-Ti_2H_{13} and (e) $C2/m$-TiH_{22}. The influence of temperature on the maximum value of the order parameter ($\Delta_{m=1}$) for selected μ^* of (c) *Immm*-Ti_2H_{13} and (f) $C2/m$-TiH_{22}. Solid circles correspond to the exact numerical solutions of the Eliashberg equations, the red and blue lines represent the results obtained using analytical formulas [Eq.10]. Black lines are predicted by BCS model [Eq.10, where Γ=3]

tions are satisfactory when λ is small (< 0.8). While, the underestimation of analytical approaches become obvious when λ is large (> 0.8). This is well within expectations that these two analytical formulas can give accurate T_c values for weak-coupling superconductors, while stop being satisfactory for strong-coupling ones. The limitation of these two analytic formulas is inherently due to the fact that they are all empirical formulas derived from the numerical solution of the Eliashberg equation of three spectra, namely Pb, Hg, and Einstein spectra; when $\alpha^2F(\omega)$ deviates greatly from these three spectra, the accuracy of the analytic formulas decreases[60]. Note that anharmonicity, which usually decreases T_c, is not included in our calculations.

The influence of pressure on T_c has been widely discussed before. Theoretical studies of some systems[5,61,62] show that T_c will decrease with increasing pressure; some[63,64] report T_c to increase with pressure; and others[65,66] reveal negligible pressure dependence. Although the values of T_c listed in Table I are not sufficient to completely determine the impact of pressure on T_c, it still can be seen that it has a negative effect on that of $C2/m$-TiH_{22}, $I\bar{4}$-Ti_5H_{14}, *Ibam*-Ti_2H_5 and $I4/mmm$-TiH, while has a positive effect on that of $P\bar{1}$-TiH_{12} and $I4/m$-Ti_5H_{13}. One possible explanation is that pressure impacts T_c by affecting the phonon softening, which can cause an increase in T_c. For example, phonon modes of $C2/m$-TiH_{22} around the A and Z points harden from 250 to 350 GPa [see Fig. 7(b) and Fig. S1(a)] and phonon modes of $P\bar{1}$-TiH_{12} around the Γ and Z point soften from 150 to 350 GPa [see Fig. S1(b) and Fig. 7(d)].

IV. CONCLUSIONS

In order to discover high-T_c superconductors, the Ti–H system at pressures up to 350 GPa was systematically explored using the *ab initio* evolutionary algorithm USPEX. A phase ($R\bar{3}m$-TiH) and several stoichiometries ($C2/m$-TiH_{22}, $P\bar{1}$-TiH_{12}, *Immm*-Ti_2H_{13}, *Fddd*-TiH_4, $I\bar{4}$-Ti_5H_{14}, $I4/m$-Ti_5H_{13} and *Ibam*-Ti_2H_5) were predicted, and found to be dynamically stable in their predicted pressure ranges of stability. With increasing pressure, $I4/mmm$-TiH transforms into $R\bar{3}m$-TiH at 230 GPa, and $I4/mmm$-TiH_2 into *Cmma*-TiH_2 at 78 GPa. *Cmma*-TiH_2 is structurally similar to $P4/nmm$-

TiH_2. $C2/m$-TiH_{22} has the highest hydrogen content among all titanium hydrides, and contains TiH_{20} cages. The estimated T_c of *Immm*-Ti_2H_{13} is 127.4–149.4 K (μ^*=0.1–0.15) at 350 GPa, which is actually higher than T_c of the aforementioned $C2/m$-TiH_{22} of 91.3–110.2 K (μ^*=0.1–0.15) at 250 GPa. Superconductivity of *Immm*-Ti_2H_{13} mainly arises from both strong coupling of the electrons with H vibrations and the large logarithmic average phonon frequency. The accuracy of three methods for estimating the T_c were compared. Taking solution of the Eliashberg equations as standard, the estimated T_c from Allen–Dynes formula is more accurate than that from the modified McMillan expression. The constructed pressure–composition phase diagram and the analysis of superconductivity of titanium hydrides will motivate future experimental synthesis of titanium hydrides and studies of their high-temperature superconductivity.

V. ACKNOWLEDGMENTS

J. M. M. acknowledges startup support from Washington State University and the Department of Physics and Astronomy thereat. A. R. O. thanks Russian Science Foundation (grant 19-72-30043) for financial support. Calculations were performed on the QSH supercomputer at Stony Brook University and institutional cluster (IC) provided by the Scientific Data and Computing Center (SDCC) at Brookhaven National Laboratory (BNL).

---

* jeffrey.mcmahon@wsu.edu

† a.oganov@skoltech.ru

[1] V. L. Ginzburg, Phys.-Uspekhi **42**, 353 (1999).

[2] D. Van Delft and P. Kes, Phys. Today **63**, 38 (2010).

[3] D. Duan, Y. Liu, F. Tian, D. Li, X. Huang, Z. Zhao, H. Yu, B. Liu, W. Tian, and T. Cui, Sci. Rep. **4**, 6968 (2014).

[4] A. Drozdov, M. Eremets, I. Troyan, V. Ksenofontov, and S. Shylin, Nature **525**, 73 (2015).

[5] H. Liu, I. I. Naumov, R. Hoffmann, N. Ashcroft, and R. J. Hemley, Proc. Natl. Acad. Sci. **114**, 6990 (2017).

[6] T. Bi, N. Zarifi, T. Terpstra, and E. Zurek, Reference Module in Chemistry, Molecular Sciences and Chemical Engineering (2019).

[7] M. Somayazulu, M. Ahart, A. K. Mishra, Z. M. Geballe, M. Baldini, Y. Meng, V. V. Struzhkin, and R. J. Hemley, Phys. Rev. Lett. **122**, 027001 (2019).

[8] A. Drozdov, P. Kong, V. Minkov, S. Besedin, M. Kuzovnikov, S. Mozaffari, L. Balicas, F. Balakirev, D. Graf, V. Prakapenka, *et al.*, Nature **569**, 528 (2019).

[9] B. Lorenz and C. Chu, in *Frontiers in Superconducting Materials* (Springer, 2005) pp. 459–497.

[10] L. Gao, Y. Xue, F. Chen, Q. Xiong, R. Meng, D. Ramirez, C. Chu, J. Eggert, and H. Mao, Phys. Rev. B **50**, 4260 (1994).

[11] N. W. Ashcroft, Phys. Rev. Lett. **21**, 1748 (1968).

[12] N. W. Ashcroft, Phys. Rev. Lett. **92**, 187002 (2004).

[13] N. W. Ashcroft, J. Phys. Condens. Matter **16**, S945 (2004).

[14] Y. Xie, Q. Li, A. R. Oganov, and H. Wang, Acta Crystallogr. C **70**, 104 (2014).

[15] X. Feng, J. Zhang, G. Gao, H. Liu, and H. Wang, RSC Adv. **5**, 59292 (2015).

[16] H. Wang, S. T. John, K. Tanaka, T. Iitaka, and Y. Ma, Proc. Natl. Acad. Sci. **109**, 6463 (2012).

[17] X. Ye, N. Zarifi, E. Zurek, R. Hoffmann, and N. Ashcroft, J. Phys. Chem. C **122**, 6298 (2018).

[18] X.-F. Li, Z.-Y. Hu, and B. Huang, Phys. Chem. Chem. Phys. **19**, 3538 (2017).

[19] Y. Liu, X. Huang, D. Duan, F. Tian, H. Liu, D. Li, Z. Zhao, X. Sha, H. Yu, H. Zhang, *et al.*, Sci. Rep. **5**, 11381 (2015).

[20] Q. Zhuang, X. Jin, T. Cui, Y. Ma, Q. Lv, Y. Li, H. Zhang, X. Meng, and K. Bao, Inorg. Chem. **56**, 3901 (2017).

[21] K. Abe and N. Ashcroft, Phys. Rev. B **88**, 174110 (2013).

[22] I. A. Kruglov, D. V. Semenok, H. Song, , I. A. Wrona, R. Akashi, M. Esfahani, D. Duan, T. Cui, A. G. Kvashnin, and A. R. Oganov, arXiv preprint arXiv:1810.01113 (2018).

[23] M. M. D. Esfahani, Z. Wang, A. R. Oganov, H. Dong, Q. Zhu, S. Wang, M. S. Rakitin, and X.-F. Zhou, Sci. Rep. **6**, 22873 (2016).

[24] J. A. Flores-Livas, A. Sanna, and E. Gross, Eur. Phys. J. B **89**, 63 (2016).

[25] X. Zhong, H. Wang, J. Zhang, H. Liu, S. Zhang, H.-F. Song, G. Yang, L. Zhang, and Y. Ma, Phys. Rev. Lett. **116**, 057002 (2016).

[26] D. V. Semenok, I. A. Kruglov, A. G. Kvashnin, and A. R. Oganov, arXiv preprint arXiv:1806.00865 (2018).

[27] H. Yakel, Acta Crystallogr. **11**, 46 (1958).

[28] A. San-Martin and F. Manchester, Bull. Alloy Phase Diagr. **8**, 30 (1987).

[29] R. S. Vennila, A. Durygin, M. Merlini, Z. Wang, and S. Saxena, Int. J. Hydrog. Energy **33**, 6667 (2008).

[30] P. E. Kalita, S. V. Sinogeikin, K. Lipinska-Kalita, T. Hartmann, X. Ke, C. Chen, and A. Cornelius, J. Appl. Phys. **108**, 043511 (2010).

[31] N. Endo, H. Saitoh, A. Machida, Y. Katayama, and K. Aoki, J. Alloys Compd. **546**, 270 (2013).

[32] K. V. Shanavas, L. Lindsay, and D. S. Parker, Sci. Rep. **6**, 28102 (2016).

[33] A. R. Oganov and C. W. Glass, J. Chem. Phys. **124**, 244704 (2006).

[34] A. R. Oganov, A. O. Lyakhov, and M. Valle, Acc. Chem. Res. **44**, 227 (2011).

[35] A. O. Lyakhov, A. R. Oganov, H. T. Stokes, and Q. Zhu, Comput. Phys. Commun. **184**, 1172 (2013).

[36] J. P. Perdew, K. Burke, and M. Ernzerhof, Phys. Rev. Lett. **77**, 3865 (1996).

[37] G. Kresse and J. Furthmüller, Phys. Rev. B **54**, 11169 (1996).

[38] See Supplemental Material at [URL will be inserted by publisher] for the composition statistic of crystal structure searching (Fig. S1); Phonon dispersion curves, phonon density of states projected onto selected atoms, Eliashberg spectral function $\alpha^2F(\omega)$, and the electron-phonon coupling parameter λ of predicted titanium hydrides at high

pressures (Fig. S2) and the calculated structural parameters (Table S1).
[39] P. E. Blöchl, Phys. Rev. B **50**, 17953 (1994).
[40] G. Kresse and D. Joubert, Phys. Rev. B **59**, 1758 (1999).
[41] A. Togo, F. Oba, and I. Tanaka, Phys. Rev. B **78**, 134106 (2008).
[42] S. Baroni, S. De Gironcoli, A. Dal Corso, and P. Giannozzi, Rev. Mod. Phys. **73**, 515 (2001).
[43] P. Giannozzi, S. Baroni, N. Bonini, M. Calandra, R. Car, C. Cavazzoni, D. Ceresoli, G. L. Chiarotti, M. Cococcioni, I. Dabo, *et al.*, J. Phys. Condens. Matter **21**, 395502 (2009).
[44] P. Giannozzi, O. Andreussi, T. Brumme, O. Bunau, M. B. Nardelli, M. Calandra, R. Car, C. Cavazzoni, D. Ceresoli, M. Cococcioni, N. Colonna, I. Carnimeo, A. D. Corso, S. de Gironcoli, P. Delugas, R. A. D. Jr, A. Ferretti, A. Floris, G. Fratesi, G. Fugallo, R. Gebauer, U. Gerstmann, F. Giustino, T. Gorni, J. Jia, M. Kawamura, H.-Y. Ko, A. Kokalj, E. Kkbenli, M. Lazzeri, M. Marsili, N. Marzari, F. Mauri, N. L. Nguyen, H.-V. Nguyen, A. O. de-la Roza, L. Paulatto, S. Ponc, D. Rocca, R. Sabatini, B. Santra, M. Schlipf, A. P. Seitsonen, A. Smogunov, I. Timrov, T. Thonhauser, P. Umari, N. Vast, X. Wu, and S. Baroni, J. Phys. Condens. Matter **29**, 465901 (2017).
[45] C. Grimaldi, L. Pietronero, and M. Scattoni, Eur. Phys. J. B **10**, 247 (1999).
[46] A. Migdal, Sov. Phys. JETP **7**, 996 (1958).
[47] J. Carbotte, Rev. Mod. Phys. **62**, 1027 (1990).
[48] P. B. Allen and B. Mitrović, in *Phys. Status Solidi*, Vol. 37 (Elsevier, 1983) pp. 1–92.
[49] R. Szczęśniak, Acta Phys. Pol. A **109**, 179 (2006).
[50] R. Szczęśniak, D. Szczęśniak, and E. Drzazga, Solid State Commun. **152**, 2023 (2012).
[51] W. McMillan, Phys. Rev. **167**, 331 (1968).
[52] R. Dynes, Solid State Communications **10**, 615 (1972).
[53] P. B. Allen and R. Dynes, Phys. Rev. B **12**, 905 (1975).
[54] K. T. Chan, B. D. Malone, and M. L. Cohen, Phys. Rev. B **86**, 094515 (2012).
[55] M. W. Chase, *NIST-JANAF Thermochemical Tables 2 Volume-Set (Journal of Physical and Chemical Reference Data Monographs)*, Vol. 2 (Wiley New York, 1998).
[56] Q. Zhuang, X. Jin, T. Cui, D. Zhang, Y. Li, X. Li, K. Bao, and B. Liu, Phys. Rev. B **98**, 024514 (2018).
[57] F. Peng, Y. Sun, C. J. Pickard, R. J. Needs, Q. Wu, and Y. Ma, Phys. Rev. Lett. **119**, 107001 (2017).
[58] G. Varelogiannis, Zeitschrift für Physik B Condensed Matter **104**, 411 (1997).
[59] M. Tortello and D. Daghero, in *Superconductors*, edited by A. Gabovich (IntechOpen, Rijeka, 2015) Chap. 8.
[60] J.-D. Cai, G.-D. Ji, H.-S. Wu, J.-H. Cai, and C.-D. Gong, Acta Physica Sinica **28** (1979).
[61] S. Yu, X. Jia, G. Frapper, D. Li, A. R. Oganov, Q. Zeng, and L. Zhang, Sci. Rep. **5**, 17764 (2015).
[62] A. G. Kvashnin, D. V. Semenok, I. A. Kruglov, I. A. Wrona, and A. R. Oganov, ACS Appl. Mater. Interfaces **10**, 43809 (2018).
[63] D. Y. Kim, R. H. Scheicher, H.-k. Mao, T. W. Kang, and R. Ahuja, Proc. Natl. Acad. Sci. **107**, 2793 (2010).
[64] Y. Li, J. Hao, H. Liu, Y. Li, and Y. Ma, J. Chem. Phys. **140**, 174712 (2014).
[65] S. Zhang, Y. Wang, J. Zhang, H. Liu, X. Zhong, H.-F. Song, G. Yang, L. Zhang, and Y. Ma, Sci. Rep. **5**, 15433 (2015).
[66] S. Zheng, S. Zhang, Y. Sun, J. Zhang, J. Lin, G. Yang, and A. Bergara, Front. Phys. **6**, 101 (2018).